As-Stiff-As-Needed Surface Deformation Combining ARAP Energy with an Anisotropic Material

Youna Le Vaou, Jean-Claude Léon, Stefanie Hahmann, Stéphane Masfrand, Matthieu Mika

As-Stiff-As-Needed surface deformation
Combining ARAP energy with an anisotropic material

Youna Le Vaou[b,c,*], Jean-Claude Léon[a], Stefanie Hahmann[b], Stéphane Masfrand[c], Matthieu Mika[c]

[a] *Univ. Grenoble Alpes, CNRS, Grenoble INP, LJK, 38000 Grenoble, France*
[b] *Univ. Grenoble Alpes, CNRS, Inria, Grenoble INP, LJK, 38000 Grenoble, France*
[c] *Groupe PSA, Centre Technique de Vélizy, 78140 Vélizy-Villacoublay, France*

Abstract

The creation of man-made shapes can be seen as the exploration of designers' 'Mental Shape Space', often supported by design reviews. To improve communication among the designers during these reviews, we introduce a new physically-based method to intuitively deform man-made shapes. This method is based on as-rigid-as possible (ARAP) shape deformation methods, known to offer a direct surface manipulation and to generate visually pleasant shapes by minimizing local deviations from rigidity. However, the organic character of ARAP shape deformations leads to undesired effects, such as surface collapsing or bulging because of an inappropriate stiffness model over the object. In this paper, we first link the designers' needs to ARAP handle-based variational mesh deformation processes. Then, we study and characterize the ARAP energy and its variants from a structural mechanics point of view. Our insight is that controlling the material stiffness could prevent the undesirable organic effects. Yet, we shed light on the fact that none of the ARAP-based methods offers an appropriate stiffness distribution over the object from a mechanical standpoint. We do so by introducing an appropriate anisotropic material, called orthotropic material, to improve the stiffness distribution over the surface and its deformation behavior for man-made shapes. This material is associated with a membrane-like structural behavior to further improve the stiffness distribution. Thanks to these settings, we derive a robust and intuitive deformation process that produces an anisotropic mesh deformation based on new edge weights in the ARAP formulation. The benefits of our new method are finally illustrated by typical design examples from the automotive industry and other man-made shapes.

Keywords: shape deformation, anisotropy, stiffness, as-rigid-as-possible, shape design, design review

*Corresponding author
Email addresses: `youna.le-vaou@inria.fr` (Youna Le Vaou), `jean-claude.leon@grenoble-inp.fr` (Jean-Claude Léon), `stefanie.hahmann@inria.fr` (Stefanie Hahmann), `stephane.masfrand@mpsa.com` (Stéphane Masfrand), `matthieu.mika@mpsa.com` (Matthieu Mika)

1. Introduction

When creating an object, designers have a mental representation of desirable shapes [1, 2, 3] that can be referred to as Mental Shape Space (MSS) in the present document. At an early design stage, designers explore and modify this MSS, notably through design reviews. In the automotive industry, design reviews are commonly performed using a 3D digital model inside a virtual reality system, where it is visualized at real-size with depth perception and realistic rendering. However, such a digital model cannot be modified in the immersive environment for lack of appropriate methods. Presently, the design review supervisor only gives feedback through verbal communication, which may lead to ambiguities [2].

Our goal is to improve communication by providing the user with a fast and efficient tool that let him/her explore new 3D shapes during the immersive design review.

Because the design review supervisor is not always a modeling expert, we need a simple interaction, and most importantly a predictable, style-preserving deformation method. As intuitive deformation methods are often applied to animation purposes [4, 5, 6, 7], they will however lead to organic shapes. To avoid losing style, a key aspect is controlling the stiffness over the model. While the idea is not new, we show in this paper that methods introducing either anisotropy from a geometric standpoint or a bending stiffness term still fail to model a predictive deformation. To obtain a satisfying behavior, our insight is to simulate a physically-based anisotropic material as part of a membrane-based structural behavior.

In this paper, we analyze from a mechanical standpoint and take into account the structural stiffness induced by a membrane model. We then add our own material stiffness through an anisotropic behavior. The compromise between these two stiffness contributions defines our method: As Stiff As Needed (ASAN) deformation. Indeed, this anisotropic behavior is simple to obtain, and we are, as far as we know, the first to make a strong connection between our proposed anisotropic deformation method and the corresponding constitutive anisotropic material law through a structural mechanics analysis.

In the following, we will connect the designer's specifications (Sect. 3) to a deformation method through both, basic principles of structural mechanics (Sect. 3.2), and an in-depth mechanical analysis of some existing deformation methods (Sect. 3.3). We work out the links between structural mechanics of real deformations of membranes or shells and the common geometric deformation models based on non linear elasticity [8, 9, 10], which allows us to introduce material anisotropy and model stiffness in a surprisingly simple manner (Sect. 4). Results, comparisons and analysis (Sect. 5) of the interactive deformation process that confirm the robustness of the proposed interaction will be provided
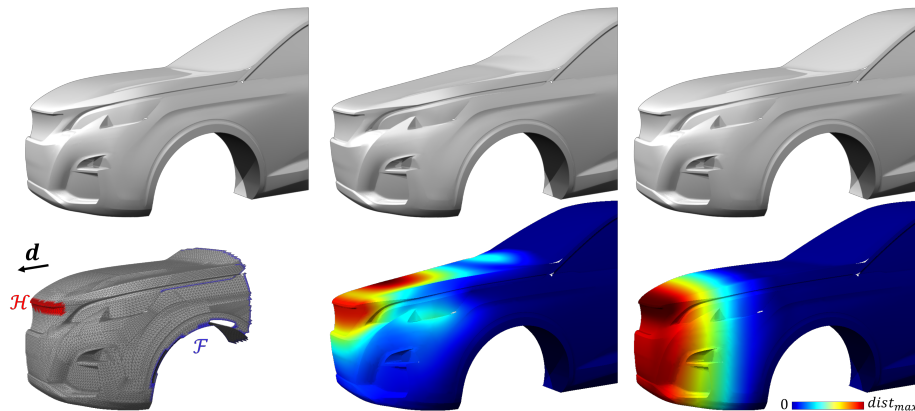
2

Figure 1: (Left) Top: Initial mesh. Bottom: Handle (red) and fixed vertices (blue) define a Region of Interest (ROI). The user defines a displacement of the handle in the direction **d** with $\|\mathbf{d}\| = 100$mm. (Middle) The initial ARAP deformation fails to preserve the shape of the hood. Bottom: Colormap of Euclidean distance to initial mesh. (Right) Our method gives a result that stays in the designers' MSS. Bottom: Colormap of Euclidean distance to initial mesh. Here, $dist_{max} = \|\mathbf{d}\|$.

using typical design examples from the automotive industry where high quality deformations are required.

2. Related Work

Letting the designers explore their MSS during design reviews is challenging because it is hard for designers to characterize explicitly the target surfaces that are part of their MSS. Giannini and Monti [11], and later Petrov [12] worked on translating emotional values, e.g., *dynamic*, *muscular*, into geometric properties. Yumer et al. [13] presented a semantic editing method. However, these contributions are still far from an exhaustive description of designers' MSS. The problem might actually be ill-posed since these emotional values are specific to each product brand, but can also depend on the current fashion and other aspects that are, as said in [11]: "recognizable and coherently understood only within specific cultural and temporal conditions". If these contributions give some insights about an MSS, they cannot be directly plugged into geometry processing requirements. Template based deformation, as proposed by Kokai et al. [14], could be another way to navigate among the MSS. However it strongly depends on the input shapes used to generate the underlying line model. Thus, the result would be too restrictive at an early design stage.

This led us to consider shape deformation from a geometry processing standpoint. A first category of approaches are deformation methods based on an auxiliary structure, like skeleton-based [7], FFD [15], curve-based [16] or cage-based [17] methods. The creation of these structures and their manipulation are however tedious and not easily applicable within a general design review scenario. A way to keep this scenario as simple as possible is to reduce the number

of user inputs. With iWires, Gal et al. [18] proposed to deform man-made shapes through automatically computed wires. However, the impact of one local change can be difficult to anticipate, due to the high number of connections between wires.

A second category of methods, based on a physically-inspired energy, seems more promising to us: they offer both plausible results and a more intuitive manipulation. The user's input can indeed be reduced to the definition of handles and displacement constraints. To process triangle meshes, the continuous energy needs to be discretized. Several strategies have been developed. Linearized versions of this energy, provide fast, robust deformation methods, but need additional techniques (multi-resolution hierarchies, . . .) to counteract linearization artifacts that appear for detailed shapes [19]. Non-linear approaches handle finite rotations or large displacements better. Sieger et al. [20] tackled the problem of shape deformation for design optimization tasks. They proposed a space-based deformation method to stay independent of the underlying model geometry and combine the energy minimization with geometric constraints. This is particularly suited for volume models. Surface models can be more efficiently processed using dedicated approaches like Sorkine and Alexa's ARAP method [8]. By minimizing local deviations from rigidity they produce appealing results looking close to physical deformations. Additionally, the handle metaphor offers an intuitive direct surface manipulation. The extended version by Chao et al. [10] improves the robustness of this method with a more precise strain energy formulation from continuum mechanics. Compared, e.g., to linear skinning techniques [7], these non-linear approaches tend to reduce deformation artifacts.

For both linear or non-linear approximations of the energy functional of the variational problem, the shape behaves as an isotropic elastic material. This rather organic behavior is not well suited for man-made shapes. For instance, the surface can collapse during deformation (Fig. 1, middle). The resulting shape leaves the designers' MSS.

To avoid this play dough effect, various approaches have been proposed. To monitor some stiffness effect of the object, Chen et al. [5] proposed to vary the size of the local neighborhood around a vertex as defined in ARAP [8], but the approach conforms to the description of an isotropic material. They also differentiate the stiffness of mesh sub-domains through a learning process. This is hardly applicable to the creative context of car body design, where the number of instances available for learning is fairly small to obtain robust results. Also, further work has been performed by Levi et al. [4, 21, 22] to extend the ARAP approach with an energy that incorporates some bending stiffness effect to improve the shape of articulated characters during their simulation movements. This requires setting the weight of this new energy term. That appeared more difficult to tune than the proposed stiffening approach. At the difference of prior works, Zhao et al., [21, 22] propose a stretching energy that will be analyzed in more details in Section 3.

Another approach is to introduce anisotropy in the deformation process, i.e. to differentiate the deformation rate along prescribed directions. Botsch and

4

Kobbelt [23] proposed to introduce such an anisotropic behavior by scaling a 2D parameterization of the region of interest (ROI). This implies however, that the direction of anisotropy depends on the shape of the 2D parameterization. Our method in contrast, takes into account the direction of deformation as well as the 3D shape of the model in order to introduce anisotropy. Colaianni et al. [24] introduced anisotropy in two existing methods (ARAP and deformation transfer [25]) by applying directly local affine transformations for each triangle of the mesh. Since the deformation process does not rely on the handle metaphor but takes place through the modification of the coefficients of these affine transformations, this approach can be qualified as indirect and is therefore not suited for design reviews.

Summary. Through the above literature review, it appears that approaches using physically-based deformation behaviors are an appropriate starting point for the design review purposes. The ARAP deformation process [8] is able to process finite rotations and large displacements. Extensions [10, 5, 4, 22] improve robustness and local stiffness, but they still fail to overcome either the surface collapsing effect and/or other undesirable side effects. To overcome this bias, anisotropy turns out to be a promising concept since it inherently incorporates the desired stiffening effects. Also, it is important to combine this stiffening process with one of the existing ARAP-type methods in order to obtain a more efficient deformation process. Before introducing our stiffening deformation process mimicking an anisotropic material and adjusting the stiffness over the model in Section 4, let us first provide in Section 3 a deeper understanding of the behavior of these physically-based deformations methods from a structural mechanics point of view to take advantage of the most appropriate one when looking for tuning stiffness distribution (see Section 4.4).

3. From the designers' specifications to a consistent deformation process

As observed through Section 2, the designers' MSS cannot be addressed directly. We rather propose to rely on physical phenomena to help defining shape deformation processes in accordance with context specific requirements expressed by designers. In particular, we focus on setting up an appropriate stiffness over the mesh to obtain a satisfactory range of shapes.

In this section, once the designer's requirements are set, we establish connections between common geometric mesh-based deformation energies and physical phenomena as studied in structural mechanics. In particular, we derive all necessary simplifying physical assumptions and recall basic concepts of structural mechanics of shells in order to better understand the observed weaknesses of existing deformations methods. The last and main contribution of this section is a detailed analysis of all existing ARAP-type methods and their comparison in terms of bending stiffness behavior in order to help define the better suited ones for being combined with the anisotropic material defined in Sect. 4.

3.1. An appropriate deformation method for design reviews

Let us first understand the main features and requirements of design reviews before selecting an appropriate model for deformation. We had the opportunity to directly interview six professional designers through informal discussions that led us to identify the *early design* as an appropriate design stage. The requirements can be summarized as follows:

(R1) **Good proportions.** Designers are looking for good proportions rather than precisely tuned surfaces. Consequently, designers are more interested in shape modifications over large areas, than on small details. For example, they want to be able to displace one area or region of interest with respect to others, to elongate or shorten areas of the object;

(R2) **Style preserving.** For example, a car hood composed of rounded convex shapes should not result in flat or even concave shape parts after a modification of its length. This implies that the prescribed displacement of some part will generally not exceed 5% of the model size;

(R3) **Predictive and context sensitive results.** For example, the displacement of a car's wheel housing should not alter its circular shape;

(R4) **Low expectations on resulting mesh quality.** The models used in the immersive environment at this stage are less detailed than later. Also, the input meshes are not always well connected. Consequently, the applied modifications should neither produce class-A shapes nor result in high-quality meshes in terms of connectivity and triangle aspect ratios;

(R5) **Intuitive interaction.** The interaction metaphor should be intuitive and handled easily and quickly;

(R6) **Reduced model preparation time.** Being able to quickly set up a design review session is mandatory, otherwise it would delay the whole design process.

When searching for an appropriate deformation method, we discarded skeleton-based, volume and space deformation methods for different reasons. Skeleton-based methods are well suited for character animation [26], but less appropriate for man-made objects. Methods based on volume or space deformations are eligible candidates since they can use geometric constraints [20], handles [27] and energies [20]. However, these deformation methods do not have a precise physical interpretation, making it difficult to remove their adverse effects. Our understanding is that the energy functionals, in order to produce predictable and context sensitive shape deformations (R3), should be strongly related to physical phenomena to take advantage of the large corpus of knowledge available in computational mechanics.

The non linear ARAP method of Sorkine and Alexa [8] and variants [10, 5, 4, 22] seem to be a relevant starting point. They indeed offer a surface-based intuitive interaction and seek to minimize local deviations from rigidity.

The choice of an appropriate interaction metaphor has to account for the above cited requirements too. The design review activity described in Section 1 justifies that the deformation process addressed be of type *push-pull rather than bending*. Indeed, the latter is more typical for the needs of character animation than for man-made shapes. Furthermore, push-pull deformations are in accordance with the shape requirements (R1) to (R3), which are calling for more careful interactions.

3.2. Structural mechanics background

This section reviews major concepts of structural mechanics helpful to better characterize ARAP-based deformation methods addressed in Section 3.3. This analysis let us understand the mechanical meaning of our algorithm, presented in Section 4.2.

Structural mechanics aims at describing the mechanical behavior of a structure through a description of its stiffness, its material properties and how they are spread over the geometric domain of the structure. The structure is herein discretized into a finite element mesh (e.g., tetrahedral, hexahedral meshes), and finite element models (FEM) [28, 29, 30] are used to study real deformations. Surface meshes as used in geometric modeling can be taken as geometric models identical to finite element ones. However, the focus of such geometric FEM-based approaches, e.g., [10, 8, 9, 4, 22], is on displacements and strains to characterize the deformation of a mesh, rather than on stresses and behavior of the materials, as is usual in structural mechanics. Our intention in this section is to determine under which simplifying hypotheses the two approaches can be connected in order to address (R1) to (R3).

The formulation of a finite element simulation can be stated as follows: let $\Omega \in \mathbb{R}^3$ be the geometric domain studied subjected to boundary conditions at some sub domain of its boundary $\partial\Omega$. These boundary conditions can be either applied forces or prescribed displacements. In the following, we will restrict these boundary conditions to prescribed displacements, in order to fit with boundary conditions commonly used in shape modeling approaches.

Notations. Under given boundary conditions, the goal is to compute solution fields, namely *displacements* $\mathbf{u}$, *strains* $\bar{\bar{\varepsilon}}$ and *stresses* $\bar{\bar{\sigma}}$, corresponding to an equilibrium state of Ω, characterized by the minimization of its internal energy. The displacement $\mathbf{u}$ is a first order tensor (vector) that expresses the displacement of each point of Ω and characterizes the deformation map.

$$\Phi : \Omega \to \Omega', \quad \Phi(\mathbf{p}) = \mathbf{q},$$

where Ω' *is the deformed configuration of* Ω and $\mathbf{u} = \mathbf{q} - \mathbf{p}$. The stress tensor $\bar{\bar{\sigma}}$ is a second order tensor expressing the forces per unit area created *inside* Ω through Φ. The strain tensor $\bar{\bar{\varepsilon}}$, also a second order tensor, is the response of Ω to given boundary conditions and is built from gradients of $\mathbf{u}$. $\bar{\bar{\varepsilon}}$ characterizes the relationship between the stresses and the strains in Ω.

Material behavior law. Let us consider the simple case of elastic behavior in three dimensions [28]. *Isotropic linear materials* which obey Hooke's law like steel and other metals can then be described by a simple linear relation in matrix form (instead of using a fourth order tensor) as:

$$\boldsymbol{\sigma} = \bar{\bar{D}}\boldsymbol{\varepsilon}, \tag{1}$$

where stresses $\boldsymbol{\sigma}$ and strains $\boldsymbol{\varepsilon}$ are vectors of 6 components, and the behavior law $\bar{\bar{D}}$ is under matrix form. A material is called *isotropic*, when its material properties have identical values in all directions in space, and *anisotropic* otherwise. Moreover, as we will see later in Section 4, that material *anisotropy* naturally introduces directional stiffness into a structure.

Medium: membranes and shells. The structure of the medium has also an impact on the material behavior: several simplifications of eq. (1) can take place depending on the morphology of Ω. Let us consider a geometry $\Omega \in \mathbb{R}^3$, where one dimension is much smaller than the two others, thus corresponding to so-called *plates* (planar structures), *membranes* and *shells* (curved structures). In this case, Ω is subjected to a planar or locally planar stress state at every point $\mathbf{p} \in \Omega$, which implies that $\boldsymbol{\sigma}$ and $\boldsymbol{\varepsilon}$ reduce to three components $[\sigma_{11}, \sigma_{22}, \sigma_{12}]^T$, and $[\varepsilon_{11}, \varepsilon_{22}, \varepsilon_{12}]^T$ (Fig. 2a). All stress components related to the normal stress along the normal $\mathbf{e}_3$ at $\mathbf{p}$, i.e., σ_{33}, σ_{23}, σ_{13}, vanish. Then, the mechanical phenomena taking place through the thickness of these media, such as bending stress distribution as illustrated in Fig. 2, can be inserted into the finite elements as part of their stiffness matrix. Under this particular formulation, the discretization of Ω reduces to a surface mesh.

Consequently, the linear behavior matrix for an elastic, isotropic material reduces to:

$$\bar{\bar{D}} = \frac{E}{(1-\nu^2)} \begin{bmatrix} 1 & \nu & 0 \\ \nu & 1 & 0 \\ 0 & 0 & (1-\nu)/2 \end{bmatrix}, \tag{2}$$

where E is the Young modulus and ν the Poisson coefficient of the material. For more details see [31, 30].

Now, membranes and shells can be distinguished based on their associated model of stress distribution assigned through the thickness t. Membranes consider normal stresses σ_{11}, σ_{22}, as constant through t (see Fig. 2c), i.e., there is no bending effect and no rotation of the sections, which simplifies even further the stiffness matrix of each finite element. Shells consider variable normal stresses σ_{11}, σ_{22} across t (see Fig. 2b) to model the bending stiffness of the structure and the rotation of the sections.

Depending on the shells thickness, two theories apply, Kirchoff-Love for thin shells and Reissner-Mindlin for thick shells [31, 30, 29] to characterize their bending stiffness. Note that Eq. (2) corresponds to the Kirchoff-Love hypothesis, where a normal and planar cross-section stays planar after deformation while Reissner-Mindlin behavior incorporates the shear modulus G of the material.
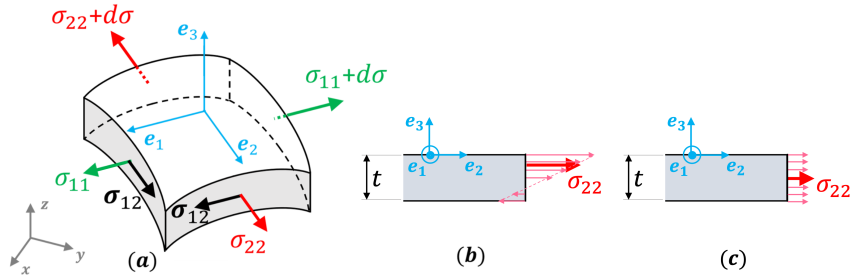
8

Figure 2: (a) Planar stress state and associated stress resultants σ_{ij} on a shell elementary domain $d\Omega$ in the local reference frame $(\mathbf{e}_1, \mathbf{e}_2, \mathbf{e}_3)$. $(\mathbf{x}, \mathbf{y}, \mathbf{z})$, global reference frame of Ω. (b) Shell and (c) membrane bending stresses of resultant σ_{22} are depicted as sets of arrows to illustrate the stress distribution across the thickness t.

Discretized strain energy. Based on the finite element mesh discretizing the structure, the internal energy E_Ω of Ω, called discretized strain energy, writes:

$$E_\Omega = \frac{1}{2} \sum_i^N \left(\int_{\Delta\Omega_i} \boldsymbol{\varepsilon}^T \bar{\bar{D}} \boldsymbol{\varepsilon} \; d(\Delta\Omega_i) \right), \tag{3}$$

where N is the number of elements. Note, that eq. (3) produces a stiffness matrix that is symmetric positive definite.

A further simplification is necessary in order to stick to geometric FEM-based deformation approaches: defining a virtual material, where the striction effect is neglected, i.e., setting $\nu = 0$. Otherwise, an undesirable lateral contraction would indeed occur when stretching the object (rubber-like squeezing behavior). This particular isotropic material reduces $\bar{\bar{D}}$ to an identity matrix, leaving E as global constant in E_Ω, which can be arbitrarily set to 1 since it has no influence from a geometric standpoint. To preserve this simplification, it means that shells models are also reduced to Kirchoff-Love behaviors, at most, since there is no geometry-based approach explicitly referring to G as in a Reissner-Mindlin behavior.

These settings are identical to the type of material characterized in Jacobson [9], Chao et al. [10] and similar ones [4, 22], when the finite element mesh is indeed a surface mesh describing Ω, and they explain why these methods exhibit a typical membrane-like behavior, also described as organic behavior.

Still, the Kirchoff-Love behavior contains stress distribution through the thickness t (Fig. 2b) that needs to be analyzed so that a second connection between structural mechanics and purely geometric approaches used in shape modeling can be established. It will help to evaluate the proximity of bending terms or bending effects in [10, 4, 22] to the mechanical shell bending model, and deliver a second explanation of adverse effects observed with ARAP-type methods.

To this end, let us address structural mechanics of shells and plates, where three concepts are distinguished through the equilibrium equations of an ele-

mentary domain $d\Omega$ (continuous case) or in the stiffness matrix of an ith finite element $\Delta\Omega_i$ (discrete case) [31, 30]:

(C1) The *membrane stress state* originates from the shell static equilibrium equations and shows that force equilibrium can be achieved with extensional, σ_{ii}, and in-place shear stress resultants, σ_{12}, (Fig. 2a);

(C2) The *bending stiffness* characterizes the extensional stress distribution across the shell thickness (Fig. 2b) or equivalently, the rotation of the cross sections when applicable with a shell theory;

(C3) The *shear stress* evolution throughout the thickness is a phenomenon that accounts for the ability of shell structures to support locally high pressures or concentrated forces. It is not the case of typical membranes, like soap bubbles that collapse when pinched under locally high pressure, e.g., with a finger.

Incorporating these concepts into a finite element framework requires the use of appropriate low order shape functions of the corresponding element. Here, we can observe a further simplification of geometric FEM-based deformation methods with respect to structural mechanics, because they commonly use linear shape functions, or so-called hat functions [9, 10, 8], defined on purely triangle meshes in graphics. Therefore, they cannot account for bending stiffness and shear stress, because either tetrahedral meshes or higher order shape functions would be required. As a consequence, they are reduced to model a *membrane behavior* (C1) with constant extensional stresses across the thickness t (see Fig. 2b) and cannot account for (C2) and (C3). And when using a membrane model with t being constant over Ω, hence $d(\Delta\Omega_i)$, t becomes a global constant in (3), and can be arbitrarily set to 1.

Up to now this section established a set of connections to linear elasticity under a set of simplifications (isotropic and linear elastic material, thin shells and linear shape functions defined on triangle meshes that define a membrane behavior). However, linear elasticity is not sufficient to model physically plausible shape behavior, when large displacements and finite rotations occur, as common in shape modeling, and as claimed by requirements (R2, R3).

Non linearity. Depending on the hypotheses on displacements and strains, the linear elasticity behavior can become non linear [29, 31].

In the simplest mechanical model, i.e., linear elasticity, displacements are considered small compared to some reference dimension d_r of Ω. For example, for a steel shell, a maximal relative displacement of $\frac{\max\|\mathbf{u}\|}{d_r} < 10^{-3}$ is considered to be small. Larger displacements involve however a stronger influence of rotations and thus, require the incorporation of geometric non linearity. This is the case in shape modeling, where it is known that large deviations from expected physical behavior may occur and cause undesired artifacts [32]. In our design review context, the amplitude of modifications also requires to take into account geometric non-linearity. In order to meet requirements (R1)-(R3) we

10

thus use a model incorporating finite rotations as in ARAP-based models.

In the next section, we therefore conduct a comparative study of existing ARAP energies, in order to figure out, which of them is the best suited for our purpose in Section 4: introducing a new surface deformation method, which, through an anisotropic material, makes the surfaces behave stiffer than before.

3.3. A comparative study of ARAP energies

Incorporation of finite rotations is the idea of ARAP-type deformation methods. Let us briefly recall their main concepts first: Sanan [33] formulates the strain energy E associated with the deformation map Φ that can be discretized and expressed on a *per vertex* basis as:

$$E(\Omega, \Omega') = \frac{1}{2} \int_{\Omega} \min_{R \in SO(3)} \|D\Phi - R\|^2 d\Omega, \tag{4}$$

where $D\Phi$ is the differential of Φ expressing the strains and R the finite rotations. (3) can be compared to (4), where (4) still expresses the strain energy in Ω under the simplifications discussed before, but clearly characterizes the contribution of the finite displacements.

Membrane-like models. Discretizing (4) in accordance to the surface mesh and taking advantage of the simplifications that occur when considering the virtual material defined in Section 3.2 ($\nu = 0$, no influence of E and t) lead to [8, 33, 4, 5]:

$$E(S, S') = \sum_{k=1}^{n_v} \min_{R_k \in SO(3)} \sum_{(i,j) \in \mathcal{E}_k} w_{ij} \|\mathbf{e}'_{ij} - R_k \mathbf{e}_{ij}\|^2, \tag{5}$$

where the factor $(\frac{1}{2})$ can be dropped since we are looking for vertex positions rather than stresses, n_v is the number of mesh vertices, R_k is the optimal rotation of the 1-neighborhood of the kth vertex, w_{ij} are the coefficients of the linear shape functions defined over each mesh edge $\mathbf{e}_{ij}$, $\mathcal{E}_k$ is the set of edges belonging to the vertex 1-neighborhood, $\mathbf{e}_{ij} \in \Omega$ and similarly $\mathbf{e}'_{ij} \in \Omega'$. Here, it is important to point out that the finite rotations considered are attached to vertices and their 1-neighborhood.

In the ARAP method as described by Sorkine and Alexa [8], $\mathcal{E}_k$ is defined by the radial edges, also called *spokes*, around vertex v_k (yellow edges in Fig. 7), hereafter designated as **ARAP-s**. As pointed out by Chao et al. [10], this setting does not incorporate all the contributions to the strain energy as defined in (4) or (3). These contributions are needed to match the non linear elastic behavior required to compare to physical phenomena. ARAP-s may lead to negative weights w_{ij} [34, 22]. Consequently, the associated matrix of Eq. (5) is no longer positive semidefinite, as required to describe either a Dirichlet energy [35] or a simplified version of a strain energy (3). The resulting behavior is no longer predictive and cannot meet (R2, R3). To solve this, Chao et al. define $\mathcal{E}_k$ by

the entire 1-neighborhood composed of radial and opposite edges, called *spokes & rims* (yellow and green edges in Fig. 7), hereafter referred to as **ARAP-s&r**.

In Zhao et al. [21, 22], starting with a slightly different parameterization of the deformation, they end up with a discretized expression of (4) where the elementary contribution is defined over edges rather than vertices, called stretching energy:

$$E(S, S') = \sum_{k=1}^{n_e} \min_{R(t_{ij}) \in SO(3)} \sum_{(i,j) \in \mathcal{E}_k} \cot a_{ij} \, \|\mathbf{e'}_{ij} - R(t_{ij})\mathbf{e}_{ij}\|^2, \qquad (6)$$

where n_e is the number of mesh edges, $R(t_{ij})$ is the optimal rotation of the trian-
gle containing the edge $\mathbf{e}_{ij}$ and a_{ij} the angle opposite to $\mathbf{e}_{ij}$. Considering Fig. 7, a_{ij} designates either α_{ij} or β_{ij} depending on the order of the vertices (v_i, v_j) defining $\mathbf{e}_{ij}$. Finally, $\mathcal{E}_k$ designates the half edges of the kth edge. Because (6) is also a discretization of (4), the corresponding stiffness matrix is positive semi-definite. As pointed out in Zhao et al. [21, 22], and also stated in Liu et al. [36]
this stretching energy measures the variation of minimum/maximum stretch-ing ratios, i.e., the strains at each point along directions in the tangent plane under Φ. Mechanically, this stretching behavior is consistent with a membrane behavior and characterized by the in-plane principal stresses (σ_{ii} in Fig. 3) or strains. Let us refer to this deformation model as **ARAP-m**.

When comparing ARAP-s&r and ARAP-m, it can be observed that (6) is closer to a non linear membrane strain energy than (5). In-deed, under membrane behavior with large dis-placements, the finite rotations characterize the
rigid body movement of each finite element and hence are attached to each mesh triangle as in (6). This is not the case with ARAP-s&r [10] in (5), where the 1-neighborhood ends up with a triangle subjected to a different rigid body rota-
tion at each of its vertices. This is interpreted in [10, 21, 22] as a stiffness effect. However, it can hardly be related to a bending stiffness

Figure 3: Car body deforma-tion using ARAP-s when negative weights appear.

since this physical phenomenon is related to a shell thickness behavior, whereas the geometric deformation models addressed here do not take into account ex-
plicitly this shell thickness mechanical behavior. Nevertheless, ARAP-s&r and ARAP-m can be regarded as the reference functional as close as possible to the description of a non linear membrane deformation behavior.

Stiffness effects. Now, let us now focus on the mechanical behavior of exten-sions of ARAP-s&r and ARAP-m, as proposed by Chen et al. [5], Levi et al. [4],
and Zhao et al. [22]. In particular, we will analyze how close their introduced stiffness effects are to some physical phenomenon like the bending stiffness. This might be of interest in order to correct the effect observed in Fig. 1 (middle). To summarize and compare these extensions, we show in Fig. 4 two simple test
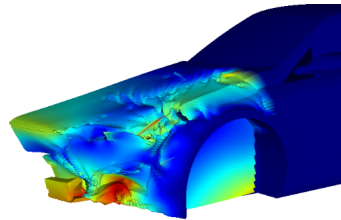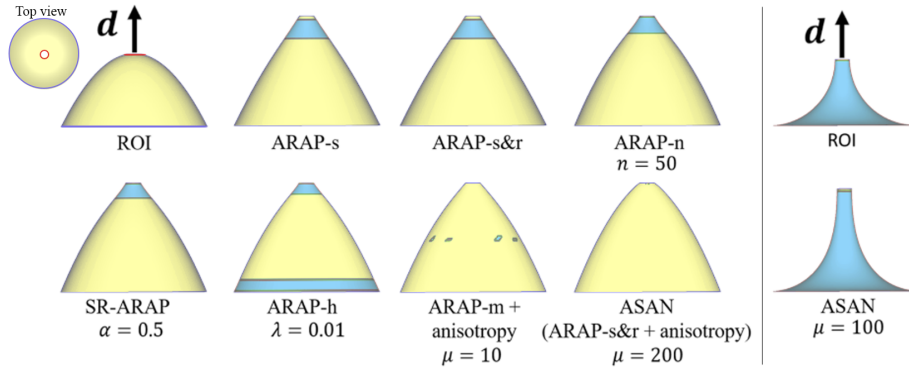
Figure 4: Comparison of ARAP-based methods using an example of a simple genus-1 structure incorporating tensile stresses. The initial shape has a strictly positive discrete Gaussian curvature. Handle is set at the top with a prescribed displacement **d**. Circular base of the model is fixed. Colors depict the discrete Gaussian curvature sign change in the deformed mesh. ARAP-based methods incorporating a control parameter have been evaluated through a variation of this parameter. Values of these parameters characterize the maximum values reached until a saturation effect was observed with as less as possible undesired curvature changes. Combining ARAP-m with anisotropy reaches its best result with $\mu = 10$. Increasing μ highlighted numerical instabilities. Combining ARAP-s&r with anisotropy (ASAN our method) produces the best results with $\mu = 200$. Right: ASAN deformation of a shape with negative Gaussian curvature.

cases which synthesize their behavior. One is an axi-symmetric dome-shaped model that exhibits strictly positive discrete Gaussian curvature. A second one (right), is an axi-symmetric hat-shaped model with strictly negative discrete Gaussian curvature. Observing and analyzing the curvature sign changes helps assessing whether the stiffness effects can be properly monitored or not. Both deformations can be achieved essentially with tensile stresses, which enables the comparison with ARAP-s too. CGAL [34] implementation of ARAP-s [8] was used. Looking at the results, it clearly appears that hat-shaped model preserved its negative Gaussian curvature with all deformation methods while the dome-shaped one exhibited differences to be analyzed. For this reason, Fig. 4 (right) illustrates only the results of our method, we are going to call it *ASAN,* on the hat-shaped model.

First of all, Chen et al. [5] take advantage of the observations made by Chao et al. [10] and Zhao et al. [21] and extend the vertex neighborhood of ARAP-s to an n-neighborhood. This extension is denoted **ARAP-n**. Even though Chen et al. [5] illustrate the *stiffening* effect of n on some test cases, applying the method to other types of models reveals side effects, especially around the handles (see Fig. 16). These adverse effects do not even vanish when increasing the neighborhood size n. A physically plausible stiffening effect should, however, act like thickening the shape and thus remove these adverse effects instead of increasing them. These adverse effects are characterized in Fig. 4 by a change of discrete Gaussian curvature sign, which does not vanish when increasing n. Figs. 16 in Sect.5 will confirm this hardly predictive behavior. ARAP-n cannot

13

be compared to mechanical bending stiffness and cannot be used alone to satisfy (R2)-(R5).

Levi et al. [4] add to (4) and to (5) a term that penalizes the rotation between two neighboring edges sets. They refer to this approach as **SR-ARAP** and consider it as bending stiffness that is governed by a parameter α weighting the penalization. SR-ARAP is built from ARAP-s&r that is regarded as a membrane strain energy and the complementary term as a bending stiffness one. Like ARAP-n, some test cases illustrate the stiffening effect obtained. However, based on the previous observations neither this membrane nor this bending stiffness energies can be close to physical phenomena that can be predictably monitored. This is also enforced when applying SR-ARAP to the test models of Fig. 4, where adverse effects similar to ARAP-n appear and increasing α does not lead to their removal either. With respect to these observations, SR-ARAP does not conform to a physical stiffness model and thus cannot be used alone to satisfy (R2)-(R5).

Zhao et al. [22] add to their ARAP-m an energy term that focuses on the variation of the discrete mean curvature during the deformation process that is also regarded as a bending stiffness. The resulting approach is an hybrid one, noted **ARAP-h**, that weighs linearly both terms. If shell structural mechanics refers to the initial curvature of the shell and to its mean curvature [30] as one of its features, it does not appear as a leading term that monitors the shell bending stiffness. Also, this is confirmed by the test cases in Fig. 4, where the parameter λ weighting the membrane and bending terms has not enough effect to correct the artifacts observed near the handle. Additionally, when λ is close to 0 to express essentially the bending energy, the deformed mesh departs from physical phenomena. The membrane behavior indeed conveys the information required to handle the large displacements, thus it can hardly vanish in a physical shell behavior. Here again, ARAP-h does not contain a stiffness model that can be used alone to satisfy (R2)-(R5).

To summarize, one can observe that the functionals closest to the membrane model, e.g., ARAP-m, ARAP-s&r, do not provide enough stiffness to avoid the surface collapse problem observed in Fig. 1. Consequently, a stiffer behavior is mandatory, but none of the functionals analyzed, ARAP-n, SR-ARAP, ARAP-h, have been able to avoid adverse effects in a deformed surface. Furthermore, the control parameter associated with each of the functionals acts globally over the mesh and has no tight connection with the mechanical bending stiffness, which makes them not predictive enough.

To avoid these phenomena, some alternatives must be considered to express and monitor the stiffness in Ω in order to better meet (R2)-(R5). A promising alternative is to use a membrane-based behavior, such as ARAP-m or ARAP-s&r, and stiffen the surface through an anisotropic material behavior law.
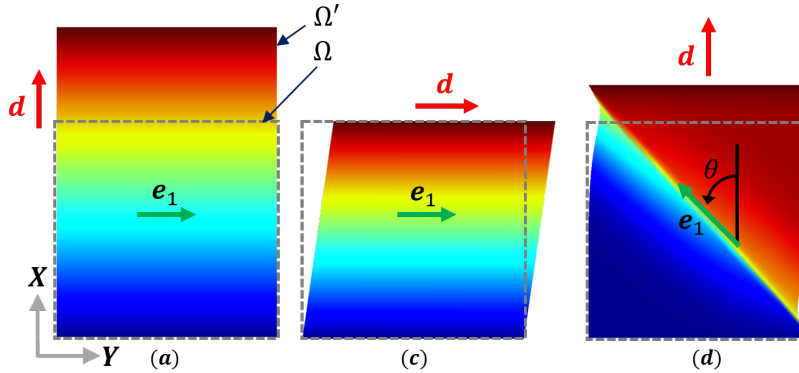
14

Figure 5: Anisotropic (orthotropic) deformation behavior. Deformation behavior of a 2D orthotropic material defined over Ω (dotted lines) with fiber direction $\mathbf{e}_1$. The top vertices are constrained to a displacement $\mathbf{d}$ and the bottom vertices are kept fixed. The prescribed displacement (load) $\mathbf{d}$ is applied orthogonal (a), parallel (b) and $\theta = 45°$ (c) to the fibers. Colormap of Euclidean distance to initial mesh vertices.

4. Stiffening a surface using an anisotropic virtual material

Section 3 has highlighted some relationships between surface deformation methods and mechanical behaviors. This has led to the selection of ARAP as a deformation method, which is close to a membrane behavior, in particular ARAP-m or ARAP-s&r. But Sect. 3 also confirmed the need for a predictable and robust stiffening method, which cannot be achieved with the already available approaches (see Fig. 4). This last point is now addressed with the introduction of an anisotropic material through two complementary steps:

- **Anisotropic constitutive material law**. Sect. 4.1 - 4.3 where we formulate and, for the first time, validate our approach from a mechanical point of view rather than from a geometrical one, which makes our method more effective and predictable;

- **Structural stiffness setting**. Sect. 4.4 where we look for the best suited stiffness distribution over Ω to combine the anisotropic material law with the structural stiffness model of either ARAP-m or ARAP-s&r, independently of the numerical instabilities of ARAP-m already observed in Fig. 4.

4.1. Anisotropic material

A material is called *anisotropic* when its elastic parameters in $\bar{\bar{D}}$ are direction dependent. For example, in a fabric, one predominant direction is given by the weft thread. In our work, we focus on a sub-type of anisotropic material: *orthotropic material*, where the directions of anisotropy are orthogonal[1] to each

---

[1]In the remaining of the paper, we consider an orthotropic behavior of a virtual material, but often call it anisotropy for the sake of simplicity.
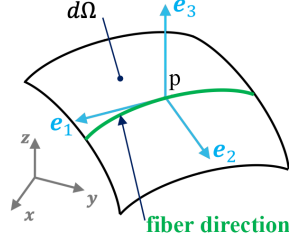
4.5cm

Figure 6: Notations: Elementary membrane domain $d\Omega$ with local *orthotropy directions* $\mathbf{e}_1, \mathbf{e}_2$ in the reference frame $(\mathbf{x}, \mathbf{y}, \mathbf{z})$ of Ω. Material fibers are aligned with $\mathbf{e}_1$.

other. In the present case of membranes or shells, an orthotropic material has two main orthogonal directions, along which its different characteristics remain unchanged. Let us first consider the medium as a unidirectional composite material where fibers are laid down parallel to each other and form the surface of the membrane or shell [37]. Let us denote the orthotropy directions by $\mathbf{e}_1$, $\mathbf{e}_2$ and let $\mathbf{e}_1$ be the one aligned with the fibers, see Fig. 6. As an example, we illustrate in Fig. 5 the elastic behavior of a 2D of orthotropic material, where we apply a load along $\mathbf{d}$ to the top boundary in either orthogonal, parallel and with 45° direction with respect to $\mathbf{e}_1$. To define an anisotropic medium, we need to redefine the constitutive law $\bar{\bar{D}}$. Considering that **the fibers are aligned with orthotropy direction $\mathbf{e}_1$** (Fig. 6), the compliance matrix[2] in the local reference frame $(p; \mathbf{e}_1, \mathbf{e}_2, \mathbf{e}_3)$ is given by:

$$\bar{\bar{D}}^{-1} = \bar{\bar{C}} = \begin{bmatrix} \frac{1}{E_1} & \frac{-\nu_{12}}{E_1} & 0 \\ \frac{-\nu_{21}}{E_2} & \frac{1}{E_2} & 0 \\ 0 & 0 & \frac{1}{2G_{12}} \end{bmatrix} \tag{7}$$

with the constraint: $\nu_{21}E_1 = \nu_{12}E_2$. Anisotropy is then characterized by five parameters: E_1, E_2 the Young's moduli along the orthotropy directions $\mathbf{e}_1$ and $\mathbf{e}_2$ set in the tangent plane at p, respectively, G_{12} the shear modulus, ν_{12}, ν_{21} the Poisson's coefficients measured when the laminate is loaded along directions $\mathbf{e}_1$, and $\mathbf{e}_2$, respectively, see Fig. 5a.

If the directions of orthotropy do not comply with the local load direction $\mathbf{d}$, or equivalently, the prescribed displacements, $\bar{\bar{D}}$, respectively $\bar{\bar{C}}$, must account for their relative angle. For simplicity, this is illustrated with the

---

[2]The compliance matrix is used here instead of $\bar{\bar{D}}$ because the matrix components take simpler forms.

2D domain of Figure 5c with $\theta \angle(\mathbf{e}_1, \mathbf{d})$ $\bar{\bar{C}}$ that becomes [37]:

$$\bar{\bar{C}} = \begin{bmatrix} \frac{1}{E_X(\theta)} & \frac{-\nu_{YX}(\theta)}{E_Y(\theta)} & \frac{\eta_{X,XY}(\theta)}{2G_{XY}(\theta)} \\ \frac{-\nu_{XY}(\theta)}{E_X(\theta)} & \frac{1}{E_Y} & \frac{\eta_{Y,XY}(\theta)}{2G_{XY}(\theta)} \\ \frac{\eta_{XY,X}(\theta)}{E_X(\theta)} & \frac{\eta_{XY,Y}(\theta)}{E_Y(\theta)} & \frac{1}{2G_{XY}(\theta)} \end{bmatrix} \tag{8}$$

with the constraints: $\nu_{YX}E_X = \nu_{XY}E_Y$ and E_X, E_Y, ν_{XY}, ν_{YX}, G_{XY} being resp. Young's moduli, Poisson's coefficients and shear modulus. However, new coefficients $\eta_{X,XY}$, $\eta_{Y,XY}$, $\eta_{XY,X}$, $\eta_{XY,Y}$ appear, representing non classical coupling between the directions $\mathbf{X}$ and $\mathbf{Y}$. Note, that these coupling coefficients indicate that adverse deformation effects can appear at a meso scale or globally over Ω when displacements are prescribed along directions differing from the orthotropy ones, (see Fig. 5c where the adverse effects entirely span Ω). These effects, which are also visible in Fig. 10 at meso scale, are however undesirable in shape modeling and must be avoided as much as possible.

Our approach. Our approach is now to propose a deformation method of type ARAP (6), based on an anisotropic material (7). To do so, for a given direction of load $\mathbf{d}$, we want to implicitly define the parameters of $\bar{\bar{C}}$ and the directions of anisotropy.

Note that a more direct approach of explicitly specifying the parameters of $\bar{\bar{C}}$ would complicate the situation. We would leave the framework of, what we called, geometric shape deformation methods based on FE [9, 38]. Let us briefly explain why: firstly, specifying the material parameters (ν_{12}, ν_{21}, E_1, E_2, G_{12}) addresses the domain Ω globally. Whereas setting the Poisson's coefficients $\nu_{12} = \nu_{21} = 0$ makes sense, to avoid lateral contraction (see Sect. 3.2), setting the material parameters E_1, E_2, and G_{12} is not intuitive neither for general public nor for the designers. Secondly, the orthotropy directions apply locally over each elementary domain $d\Omega$, see Fig. 5(a). In other words, ($\mathbf{e}_1$, $\mathbf{e}_2$) vary from one element (mesh triangle) to another, and the corresponding stiffness matrix of each element differs. Consequently, if we were to define $\mathbf{e}_1$, $\mathbf{e}_2$ independently for each triangle, the simplifications obtained in the global stiffness matrix that led to the connections with FE-based geometric methods [9, 38] would no longer hold.

4.2. Generating anisotropic material parameters using a geometric approach

Before explaining how we set the anisotropy parameters, let us fix the notations and recall the framework of our approach as it was motivated in detail in Sect. 3.3. Firstly, our goal is to introduce anisotropic material behavior into a membrane-like structural behavior. We can use either ARAP-s&r [10] or ARAP-m [22] in order to ensure convergence and adequacy with the mechanical principles developed in Section 3. Secondly, we adhere to the *handle metaphor* when translating the designer's push/pull action onto the mesh. The designer interactively pre-defines a set of handle vertices and a region of interest (ROI)

17

in the input triangular mesh. The ROI defines the geometric domain Ω. Its boundary vertices, denoted $\partial\Omega$, are supposed to stay fix. A displacement $\mathbf{d}$ is applied to the handle vertices, which together with fixed $\partial\Omega$ define the boundary conditions of the mesh deformation process. Thus $\mathbf{d}$ drives the displacement of each mesh vertex $\mathbf{p} \in \Omega$ and characterizes the deformation process.

Anisotropy is used to introduce a direction dependent stiffening effect into the surface by keeping it flexible in other directions. We want the deformation process being predictive and style preserving. Our assumption is therefore, that the surface better preserves its initial shape, when no lateral contractions (surface collapsing effects) occur during deformation. In other words, the surface's cross sections perpendicular to the push/pull direction $\mathbf{d}$ should stay as rigid as possible, while the surface deforms in direction $\mathbf{d}$. This is exactly what an anisotropic material can ensure. Then it becomes obvious, *that the anisotropy directions and so the stiffness should depend on the user's action*, i.e. on its push/pull direction $\mathbf{d}$. Otherwise, if the directions of anisotropy were related to geometric characteristics, as in Botsch et al. [23], the deformation would depend on the ROI geometry rather than a physically-based behavior. The deformation would be unpredictable or inadequate wrt user's requirements.

Since in this process the user's push/pull direction $\mathbf{d}$ has this prominent role of predictably stiffening the cross sections, we define an *apparent direction of orthotropy* $\mathbf{d}_o$ and set it $\mathbf{d}_o := \mathbf{d}$. Other choices are conceivable, but not recommended, see Section 4.4 and Fig. 5(c). Note, that we define this direction globally over Ω in 3D while local orthotropy directions for each triangle are indirectly deduced (see Sect. 4.3.4).

We now define the orthotropy parameters for each triangle $\mathcal{T} \in \Omega$ (Ω being the user-defined ROI) by introducing new *anisotropic cotan-weights*. These weights will act as stiffness parameters, since they implicitly set the material coefficients, the ratio $E_1/E_2, \nu_{12}, \nu_{21}$, and G_{12}, accordingly, as we will verify in Section 4.3. The algorithm is the following:

1- Choose the apparent direction of orthotropy $\mathbf{d}_o := \mathbf{d}$.

2- Define a linear transformation τ along $\mathbf{d}_o$ applied to Ω

$$\tau : \Omega \to \bar{\Omega}, \quad \mathbf{p} \mapsto \bar{\mathbf{p}} = \mathbf{p} + \frac{(\mu - 1)(\mathbf{p} . \mathbf{d}_o)}{\|\mathbf{d}_o\|^2}\mathbf{d}_o. \tag{9}$$

τ stretches Ω along $\mathbf{d}_o$ with a scaling factor $\mu > 1$.

3- Compute new anisotropic weights $w_{ij}^{aniso} = \frac{1}{2}(\cot(\tilde{\alpha}_{ij}) + \cot(\tilde{\beta}_{ij}))$ from the scaled mesh $\bar{\Omega}$, see notations in Fig. 7(a). These weights w_{ij}^{aniso}, which are associated to the edges $\mathbf{e}_{ij}$, are coefficients derived from the stiffness matrix of $\mathcal{T}$ (here regarded as a finite element) [9]: the higher w_{ij}^{aniso} will be, the stiffer the edge $\mathbf{e}_{ij}$ will behave. For example, if the edge $\mathbf{e}_{ij}$ is perpendicular to the displacement direction $\mathbf{d}$, the angles α_{ij} and β_{ij} will become thinner, leading to a higher weight. In other words, *the sections perpendicular to $\mathbf{d}$ become stiffer*.
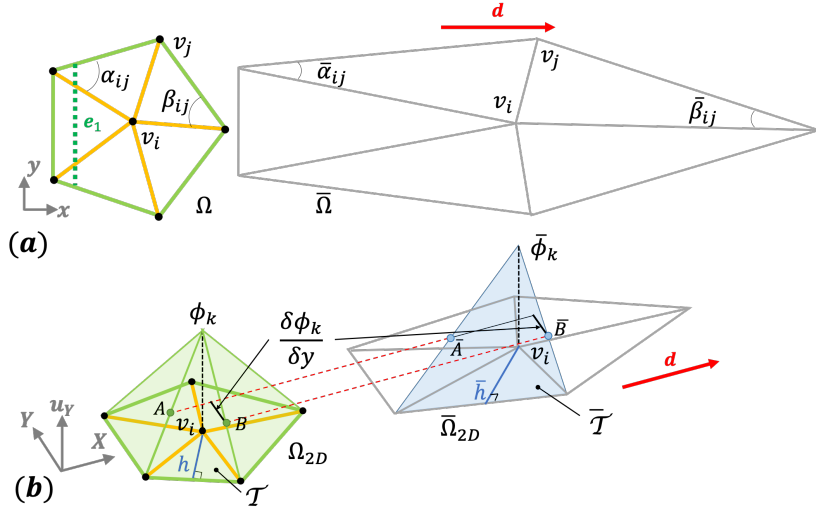
18

Figure 7: (a) Stretching Ω changes the cotangent weights of a vertex neighborhood and sets the stiff direction $\mathbf{e}_1$ (Schematic view on a 3D vertex neighborhood). (b) Hat function or, equivalently shape function, ϕ_k subjected to $\tau : \phi_k \mapsto \bar{\phi}_k$ defined from $\mathbf{d}_o$, $\bar{\phi}_k$, and associated with Ω_{2D}. ϕ_k contributes to the Y component u^Y of displacement vector $\mathbf{u}$. Illustration of the influence of τ: the strain along $\mathbf{Y}$ is null $(\mathbf{AB}.\mathbf{Y} = \bar{\mathbf{A}}\bar{\mathbf{B}}.\mathbf{Y})$, whereas τ linearly modifies the strain along $\mathbf{d} = \mathbf{X}$.

4- Assign w_{ij}^{aniso} to each edge $\mathbf{e}_{ij} \in \Omega$ and apply either the ARAP-m or the ARAP-s&r functionals, i.e., minimize $E(S, S')$ in (6) or (5).

This setting defines an anisotropic behavior. The anisotropy of Ω sets a high stiffness orthogonally to $\mathbf{d}_o$, but a much lower one along $\mathbf{d}_o$. Figuratively speaking, Ω behaves as a laminate with unidirectional fibers along $\mathbf{e}_1$ where $\mathbf{e}_1$ is a local orthotropy direction defined in each triangle of Ω, and $\mathbf{e}_1 \perp \mathbf{d}_o$.

The modification of the cotan weights through the transformation τ in (9), looks like a surprisingly simple setting. It is our next contribution to show, that it is just the right way to define an effective anisotropic material in accordance with the relationships between structural mechanics as in (7) and ARAP-based deformations derived in Sect. 3.2, i.e., w_{ij}^{aniso} fits with the description of a continuous anisotropic medium whose stiffness is discretized over Ω.

4.3. Analysis and validation

Let us show that these new weights actually define an anisotropic material in coherence with (7).

4.3.1. Setting of ν_{12} and ν_{21}

We need to have $\nu_{12} = \nu_{21} = 0$, otherwise, an undesirable lateral contraction would occur when stretching the object (rubber-like squeezing behavior). Remember that the coefficients w_{ij} in ARAP methods (5) or (6) define an isotropic

19

and homogeneous material with a Poisson's coefficient $\nu = 0$ (Sect. 3.2, Paragr. *Discretized strain energy*). So, we only have to show that the application of τ preserves the same property, i.e., that it effectively sets $\nu_{12} = \nu_{21} = 0$.

Without loss of generality, let us consider Ω as a 2D domain $\Omega_{2D} \subset \mathbb{R}^2$ and the displacement $\mathbf{u}_i$ at vertex v_i under loading conditions as defined in Figure 5(a), i.e. $\mathbf{d} := \mathbf{X}$. Under this setting, the striction effect takes place along the Y component. Consequently, strains along direction $\mathbf{Y}$ monitor this phenomenon and they are analyzed hereafter. ARAP methods (5) or (6) and their associated w_{ij} produce null displacements along that direction for an isotropic material, i.e., null strains along that direction at every vertex v_i, $\varepsilon_{iYY} = 0, \forall i$ [28] leading to $\nu = 0$. The material anisotropy must not alter that property or, equivalently, the transformation $\tau : \Omega_{2D} \to \bar{\Omega}_{2D}$ should not modify that property. An analysis of the influence of τ is now performed and an illustration is given in Fig. 7(b). For that purpose, let us consider the displacement $\mathbf{u}_i$, now noted $\mathbf{u} = (u^X, u^Y)$, at an arbitrary vertex v_i. $\mathbf{u}$ is a linear combination of basis linear hat functions ϕ_k (more details in [9]) around v_i. The only component that contributes to ε_{iYY} [28] is the Y-component of $\mathbf{u}$: $\varepsilon_{iYY} = \frac{\partial u^Y}{\partial Y}$. u^Y is represented as a height field in Fig. 7(b) and $\mathcal{T} \in \Omega_{2D}$ is the triangle associated with ϕ_k at v_i with $\tau : \mathcal{T} \mapsto \bar{\mathcal{T}}$. Also, $\bar{u}^Y = \tau(u^Y)$.

Because ϕ_k is linear, τ is defined with $\mathbf{d} = \mathbf{X}$ and $\mathbf{Y}$ is orthogonal to $\mathbf{X}$, we get $\bar{\phi}_k = \tau(\phi_k)$ and ϕ_k have identical variations along $\mathbf{Y}$, see (9). This property is illustrated in Fig. 7(b) where we focus on two points $(A, B) \in \phi_k$ and their image through τ, $(\bar{A}, \bar{B}) \in \bar{\phi}_k$: for all k we have $\frac{\partial \bar{\phi}_k}{\partial Y} = \frac{\partial \phi_k}{\partial Y}$. Since u^Y is a linear combination of ϕ_k, we also have $\frac{\partial \bar{u}_k}{\partial Y} = \frac{\partial u_k}{\partial Y}$. This is equivalent to state, that τ has no effect over the displacement of v_i along $\mathbf{Y}$. **The above analysis holds for all vertices $v_i \in \Omega$, which validates the property that τ is setting $\nu_{12} = \nu_{21} = 0$.**

We have conducted a simple numerical test with an arbitrary mesh on a 2D domain Ω as illustrated in Figure 5(a). We computed a deformation of an anisotropic material by choosing the same setting as advocated in our algorithm: $\mathbf{d}_o = \mathbf{d}$ and $\mathbf{d}_o \perp$ to the fibers $\mathbf{e}_1$ (representing the stiff sections). As expected, no striction behavior occurs. The material defined using τ is such that $\nu_{12} = \nu_{21} = 0$.

The above analysis and numerical tests were performed with Ω_{2D} where its orthotropy directions are aligned with the $\mathbf{X}$ and $\mathbf{Y}$ directions of the reference frame, which directly relates to (7). The generalization to arbitrary configurations where local orthotropy directions vary and are arbitrary set w.r.t. the reference frame follow directly from the characterization of local and apparent orthotropy directions obtained at Sect. 4.3.4.

4.3.2. Setting of G_{12}

Using the same 2D domain Ω and reiterating a numerical test when prescribing a displacement along direction $\mathbf{d} = \mathbf{e}_1$ generates a shear stress characterizing G_{12}, see Fig. 5(b). Looking at the angle between $\mathbf{e}_2$ and the deformed configuration of $\mathbf{e}_1$ in Ω'_{2D}, one can observe that it is constant over Ω'_{2D}. This is confirmed

by the smooth displacement map of Fig. 5(b). **Indeed, this shows that τ generates a non zero shear modulus G_{12} that is uniformly set over Ω.** The same setting applies to an arbitrary domain Ω. This is consistent with the mechanical behavior described by (7) as desired.

4.3.3. Setting of the stiffness ratio E_1/E_2

A high stiffness ratio corresponds to a smaller strain in direction $\mathbf{e}_1$ than in direction $\mathbf{e}_2$. To avoid the surface collapsing due to the membrane behavior, we want a high stiffness ratio E_1/E_2, i.e., a strain that is much smaller in direction $\mathbf{e}_1$ than $\mathbf{e}_2$. In the following we show that this property is expressed by τ.

To this end, let us study what happens in the direction $\mathbf{d}$ by using again the 2D illustration of Figure 7(b) with Ω_{2D}. $\mathbf{d}$ is here aligned with the X-axis. We know [9] that the magnitude of the gradient of the shape function ϕ_i is inversely proportional to the height h of each triangle $\mathcal{T}$ around v_i. When τ is applied, we see here that the triangles of Ω are elongated in the direction $\mathbf{d}$, leading to an increase in their height $\bar{h}$ and thus to a decrease of the gradient of ϕ_i along the X-axis.

Now, let us show in the reference frame $(\mathbf{X}, \mathbf{Y})$ that τ generates a variation of E_X w.r.t. E_Y and that it can be related to the variation of E_1/E_2. Combining this observation with those of Sect. 4.3.1, where the gradient of ϕ_i along the Y-axis is kept unchanged under the application of τ, shows that the strains ε_{YY} behave as the homogeneous material initially defined using (5) or (6), while the strains ε_{XX} along the X-axis get larger, as observed above. As a result, it means that for a given stress state at any point of Ω_{2D}, the strains at that point vary in accordance with the direction considered. The material being linear elastic (see Sect. 2, stresses vary linearly w.r.t strains), this variation of ε_{XX} with respect to ε_{YY} shows that the Young's modulus E_X differ from E_Y (see (8)). **This difference appears when τ is applied and E_X/E_Y is monitored by μ.**

Finally, considering Figure 5(a) where Ω reduces to a simple planar square domain, and the direction of fibers $\mathbf{e}_1$ is uniformly set over Ω, Ω is subjected to a traction along $\mathbf{d} = \mathbf{X}$. There, τ and its associated parameter μ reduce the value of E_X compared to E_Y and the stress state of Ω_{2D} is uniform, i.e., the values of E_X and E_Y are constant over Ω. Indeed, $\forall \mathbf{p} \in \Omega$, E_Y is the highest value of Young's modulus because τ has no effect on ϕ_i along the Y-axis. Then, referring to the concept of principal directions of a stress state at $\mathbf{p}$ [28] and to the principal stresses, X-axis is a principal direction and E_X can be identified with E_2 in (7) because Ω is subjected to unidirectional traction state along $\mathbf{d}$. The principal directions are mutually orthogonal at $\mathbf{p}$ [28], thus Y-axis is the other principal direction and E_Y can be identified with E_1 in (7). **μ monitors the ratio E_1/E_2.**

4.3.4. Setting of local orthotropy directions

Section 4.3.3 has started to refer to the principal directions associated to a stress state. Indeed, in Figure 5(a) the principal directions at p extend over Ω into lines parallel to axes-X and Y because Ω is planar and the traction applied preserves its planarity. These lines are indeed the orthotropy lines characterizing
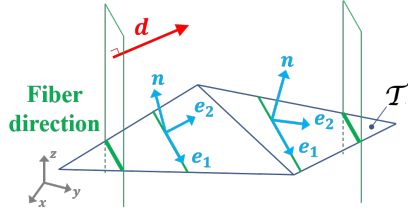
21

Figure 8: Local orthotropy directions $\mathbf{e}_1$, $\mathbf{e}_2$ derived from $\mathbf{d}$. The apparent direction of orthotropy attached to the fibers and $\mathbf{e}_1$ is featured in green.

the constitutive material of Ω. They can be designated as apparent orthotropy directions to be distinguished from the local ones $\mathbf{e}_1$ and $\mathbf{e}_2$. This particular and simple setting derives from the simple shape of Ω and the setting of τ defined with $\mathbf{d}_o := \mathbf{d} := \mathbf{X}$.

Now, let us consider a general setting to characterize the layout of the apparent orthotropy directions of the constitutive material defined using (7). τ defined by $\mathbf{d}$ sets the local orthotropy direction $\mathbf{e}_1$ within each triangle $\mathcal{T}$, such that $\mathbf{e}_1.\mathbf{d} = 0$ and $\mathbf{e}_1.\mathbf{n} = 0$, where $\mathbf{n}$ is the normal of $\mathcal{T}$. Then, propagating this setting to each triangle of Ω leads to a local apparent direction of orthotropy defined as planes orthogonal to $\mathbf{d}$ intersecting Ω (see green lines in Fig. 8). These intersections define the lines of this apparent direction over Ω, which are nothing else than the section curves of Ω orthogonal to $\mathbf{d}_o$. This apparent direction sets also $\mathbf{e}_1$ locally as a principal direction because large values of μ and $\nu_{12} = \nu_{21} = 0$ leave these lines rigid, i.e., normal stresses along this direction are extremal. $\mathbf{e}_1$ being a local principal direction, $\mathbf{e}_2$ is defined by $\mathbf{e}_2.\mathbf{e}_1 = 0$, $\mathbf{e}_2.\mathbf{n} = 0$. $\mathbf{e}_2$ defines the second local orthotropy direction and the corresponding lines of apparent direction of orthotropy over Ω. Figure 8 depicts the layout of these local directions. Their definition being based on the stress state at every point $\mathbf{p} \in \Omega$, their setting over a continuous domain is continuous and their piecewise representation over Ω is solely influenced by its discretization.

Thus, using the coefficients w_{ij}^{aniso} of $\bar{\Omega}$ as stated in Section 4.2 amounts to letting Ω deform more easily along $\mathbf{d}$ while preserving the sections orthogonal to $\mathbf{d}$.

Summary of the validation. Our approach enables a smooth distribution of material parameters and orthotropy directions over Ω that is indeed transparent for the user. The material parameters set are conform to (7) and μ is the only parameter left to monitor the relative stiffness along the apparent orthotropy directions. If the orthotropy direction d_o is aligned with $\mathbf{d}$, then the desired orthotropic behavior is achieved, i.e. Ω becomes stiffer in planar sections orthogonal to $\mathbf{d}$. Our choice of weights w_{ij}^{aniso} combined with ARAP-m or ARAP-s&r thus defines an anisotropic behavior for membranes under large displacements and finite rotations. The collapsing effect of the surface is therefore reduced, as shown by the results in Sect. 5.

22

4.4. As Stiff As Needed deformation

Section 4.3 has shown that τ effectively defines an appropriate orthotropic material. This material provides Ω with directional stiffness, and rather than keeping a model completely rigid, makes it stiff enough to meet designers' requirements (R1)-(R3). Three choices still remain to set our method completely: the mechanical structure to combine with the anisotropic material, the value of the μ parameter monitoring the anisotropy, and the apparent orthotropy direction $\mathbf{d}_o$.

Here, the anisotropic material has to be considered as a contributor to a mechanical structure, which also has its own stiffness. The resulting deformation is a combination of the stiffness effects from both this structure and its anisotropic material. We saw in Sect. 3.3 that either ARAP-m or ARAP-s&r defines membrane-like mechanical structures. However, comparing the results obtained with ARAP-m and ARAP-s&r shows that ARAP-m exhibits some adverse effects (Fig. 9b) whereas ARAP-s&r gives satisfying results (Fig. 9c). This behavior difference derives from the fact that ARAP-m is the closest of the ARAP methods to a membrane behavior, and it is more sensitive to meso scale effects when combined with anisotropy, whereas ARAP-s&r already contains some bending stiffness effect and behaves better (see Sect. 3.3). The combination between the structural stiffness offered by ARAP-s&r and the anisotropic behavior of the material lead to our As-Stiff-As-Needed (ASAN) deformation.

Having selected ARAP-s&r as reference membrane-like behavior still leaves the setting of μ open. We observed that using large values of μ raises numerical stability issues. As a trade-off between numerical issues and amplitudes of user-prescribed displacements (see Sect. 3.2), a value $\mu = 100$ can be used independently of the shape of Ω. Consequently, the ASAN deformation method becomes entirely determined with parameter $\mathbf{d}_o$.

Up to here, we let $\mathbf{d}_o := \mathbf{d}$, i.e., the pulling direction defines the apparent orthotropy directions. At first glance, setting $\mathbf{d}_o$ independently from $\mathbf{d}$ could also be considered. However, Figure 5 and equation (8) show that adverse effects may arise at the scale of Ω when $\mathbf{d}_o$ and $\mathbf{d}$ differ. The reason for this behavior is the non-zero coupling coefficients $\eta_{X,XY}$, $\eta_{Y,XY}$, $\eta_{XY,X}$, $\eta_{XY,Y}$, which occur in the material behavior law (8). Figure 10 illustrates what happens with a complex 3D model. We chose $\angle(\mathbf{d}_o, \mathbf{d}) = 45°$ (left) and $\angle(\mathbf{d}_o, \mathbf{d}) = 90°$ (right). The top row shows the sections orthogonal to $\mathbf{d}_o$, which are indeed stiffened by our algorithm via the transformation τ (9). In all of our experiments, the results are quite similar: expected though user-undesired shape deformation occurs, e.g., in Fig. 10-left the silhouette of the front part of the car tilts forward, in Fig. 10-right the front part deforms abnormally and another artifact at global scale occurs above the wheel. These observations confirm our choice of $\mathbf{d}_o := \mathbf{d}$ as the best one for an intuitive deformation.

The ASAN deformation method, as set up with the above parameters satisfies requirements (R1-R5) as desired.
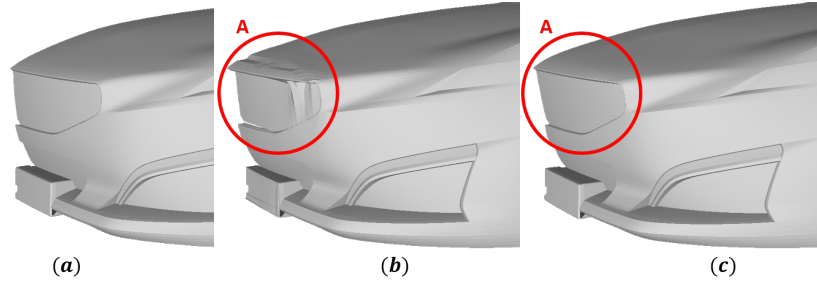
23

Figure 9: Adverse effects observed around the handle. (a) intial shape of Ω subjected to the elongation $\mathbf{d}$. (b) Adverse effects around the handle in area A obtained with ARAP-m. (c) Results obtained in area A with ARAP-s&r.
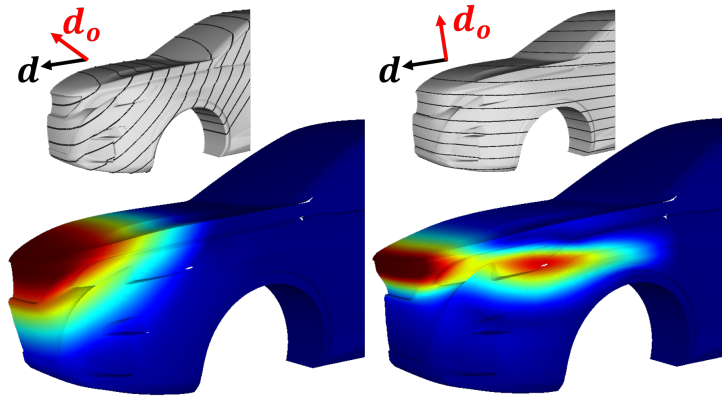

Figure 10: Anisotropy direction $\mathbf{d}_o$ decoupled from the displacement direction $\mathbf{d}$.

5. Results

After having entirely specified and characterized the mechanical behavior of the deformation process, let us briefly describe the interaction metaphor and analyze our deformation results.

770 ***Interaction & implementation.*** The user interacts with the model through the intuitive handle metaphor [23, 39], thus defining a handle region $\mathcal{H}$ and a fixed region $\mathcal{F}$. These parameters define the boundary conditions of the underlying deformation method. The corresponding ROI is computed using a breadth-first search from the handles, stopping either when meeting a vertex of 775 $\mathcal{F}$ or when a maximum distance from the handles is reached. This ROI defines the extent of the deformation area Ω. Working with an ROI has two advantages. Firstly, it reduces the computation time and, secondly, makes the deformation more predictable since localized. To initiate a deformation, the user pushes (in a position $\mathbf{p}_0$) and releases (in a position $\mathbf{p}_1$) the (possibly immersive) controller.
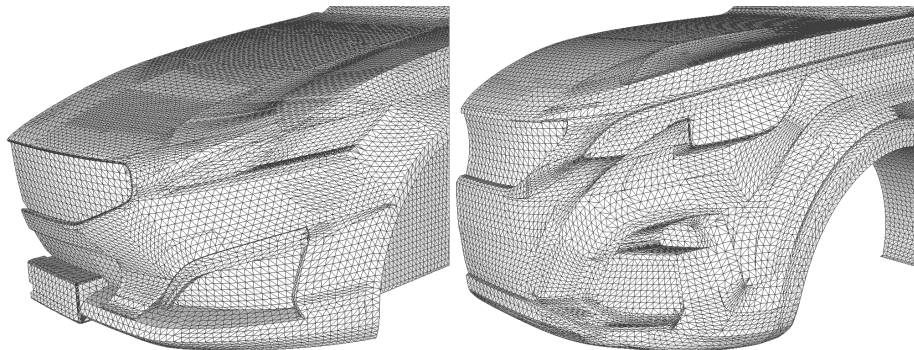
24

Figure 11: Close up on the meshes of our two car models used in Fig.s 1, 10, 12a, and 12b.

Then, $\mathbf{d} := (\mathbf{p}_1 - \mathbf{p}_0)$ defines the displacement vector of $\mathcal{H}$. We implemented our deformation method based on the LibIGL library [40].

Criterion for deformed surface evaluation. Sect. 2 points out that the characterization of designers' MSS is not currently applicable [11, 12, 13] and availability of numerous professional designers is not tractable to address a statistical analysis of results. We therefore use the sign of the Gaussian curvature as evaluation criterion. Its variations can help characterize surface undulations while avoiding to concentrate on the precise distribution of curvature values. Complementary, the comparison of maps between initial and deformed configurations contains also qualitative issues that help take into account (R2). We also display all our results with a colormap of displacements' magnitude in order to allows a quantitative comparison.

Results and comparisons. We present deformation results obtained from several industrial models. As the ASAN deformation is independent on the tessellation of the mesh, we only need to connect the patches. This feature is available in industrial solutions, which let us quickly prepare the model, meeting (R6). The models correspond to different design phases, early one (Fig. 12c) and intermediate ones (Fig. 11), with more details. It is thus possible to show the benefits of the defined stiffness distribution and the robustness of the ASAN deformation. The deformations derive from actual queries during design reviews and informal discussions with designers. In this context, the deformation amplitude $\|\mathbf{d}\|$ ranges from 50 to 100 mm, for a car length of 3 to 4.5 m, while the ROI has an extent of over 1 m. This amounts to a 10% deformation amplitude w.r.t. the ROI.

In Fig. 12, for all test cases, we show the initial model with $\mathcal{H}$, $\mathcal{F}$, the ROI, and then compare ARAP-s&r [10] energy conforming to (5) with our ASAN deformation. The colormap in the left column encodes the displacement of mesh vertices wrt the initial mesh. The right column visualizes the sign of the Gaussian curvature, positive values (yellow) and negative values (blue).

25
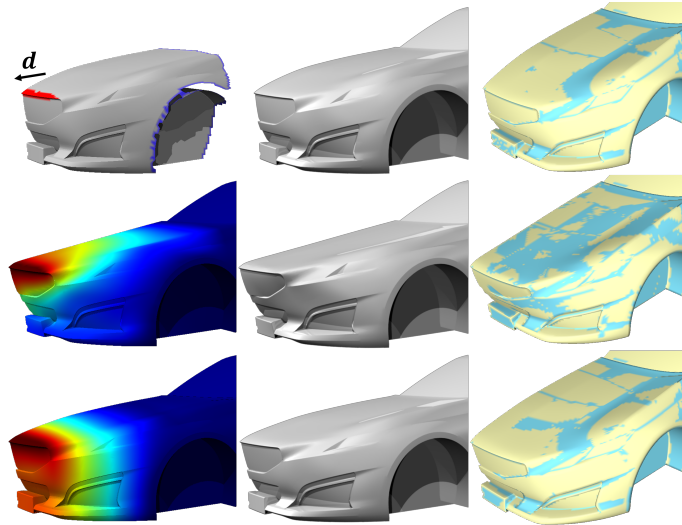
(a) Elongation of the hood ($\|\mathbf{d}\| = 100$mm).
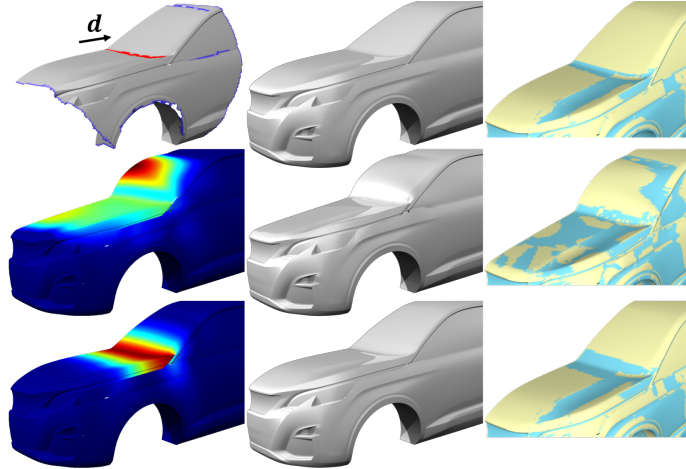
(b) Modification of the slope of the windshield ($\|\mathbf{d}\| = 55$mm).
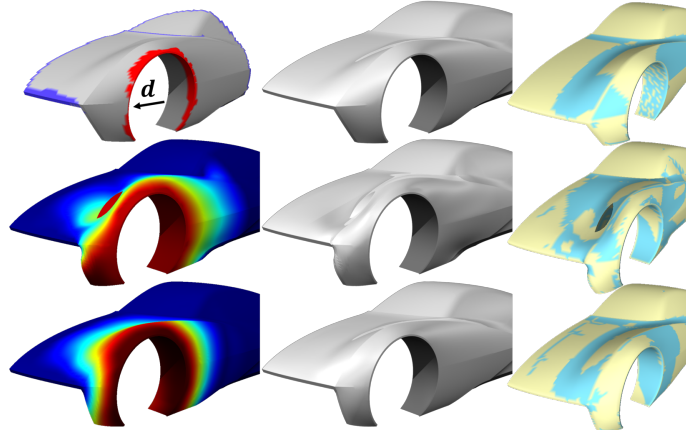
(c) Displacement of the wheel housing ($\|\mathbf{d}\| = 110$mm).

Figure 12: Within each image (a,b,c): (Top row) ROI with $\mathcal{H}$, $\mathcal{F}$ and $\mathbf{d}$, followed by the initial model (Middle row) Results with ARAP-s&r; (Bottom row) ASAN deformation method. (Left column) Color plots of the Euclidean distance between Ω and Ω'; (Right column) Curvature color plots showing the sign of the Gaussian curvature: positive curvature (yellow), negative curvature (blue).
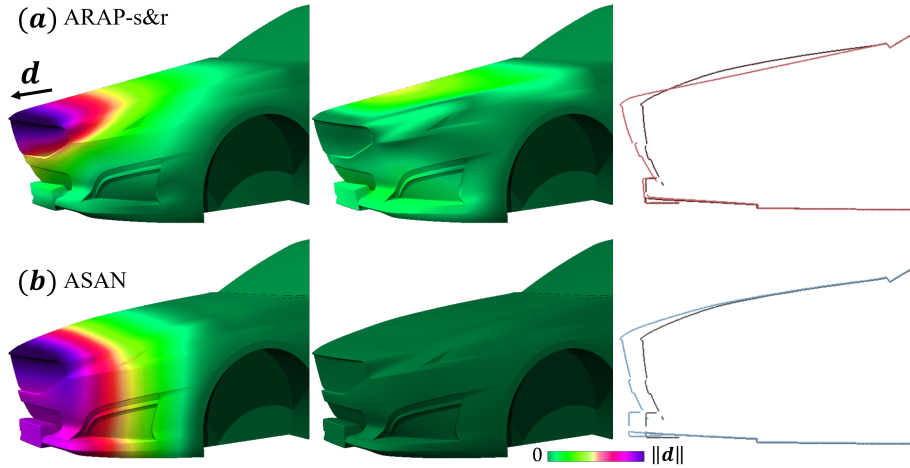
Figure 13: Decomposition of the displacement components for the elongation of the hood ($\|\mathbf{d}\| = 100$mm). Color plot of the projection of the Euclidean distance between Ω and Ω' along $\mathbf{d}$ (left), onto planes orthogonal to $\mathbf{d}$ (middle), and section curves showing the silhouette of the car before (black curve) and after (color curve) the deformation (right).

Shape preservation. Figure 12 illustrates the shape preserving property of ASAN and compares to ARAP-s&r using 3 different car models and 3 different deformations. The first example, Figure 12a, demonstrates that the initial shape of the hood as well as the sharp details in the front are well preserved with ASAN deformation. In the second example, Figure 12b, the focus is on the windshield and the hood. In the third example, Figure 12c, the wheel housing is displaced. In all three examples, the color plots (left column) show precisely where the displacements occur and how they are distributed. Wheras the ASAN displacements are localized and smoothly decreasing following the section planes orthogonal to the pulling direction $\mathbf{d}$, the ARAP-s&r exhibits in Fig. 12a undesired flattening of the hood, in Fig. 12b a stretching of the hood on one side and an inflation of the windshield on the other one, and in Fig. 12c again some undesired localized artifacts.

The sign map of Gaussian curvature (right column) highlights the shape-preserving property qualitatively. Indeed, with ARAP-s&r all observed surface collapsing effects are highlighted with a frequently changing curvature sign. On the contrary, the maps obtained for ASAN show a similar curvature profile, where locally convex surface parts stay convex, idem for hyperbolic ones.

Anisotropic stiffness. As shown in Figure 12 (colormaps left), the ASAN deformation generates the desired anisotropic deformation behavior: the deformation acts essentially in direction $\mathbf{d}$ and preserves the sections orthogonal to $\mathbf{d}$. In complement, we visualize in Fig. 13 in which direction the displacements occur. To this end we decompose each displacement vector into a component in direction $\mathbf{d}$ and a component in the plane orthogonal to $\mathbf{d}$. With ARAP-s&r, displacements occur inside the sections planes Fig. 13(top, middle), which
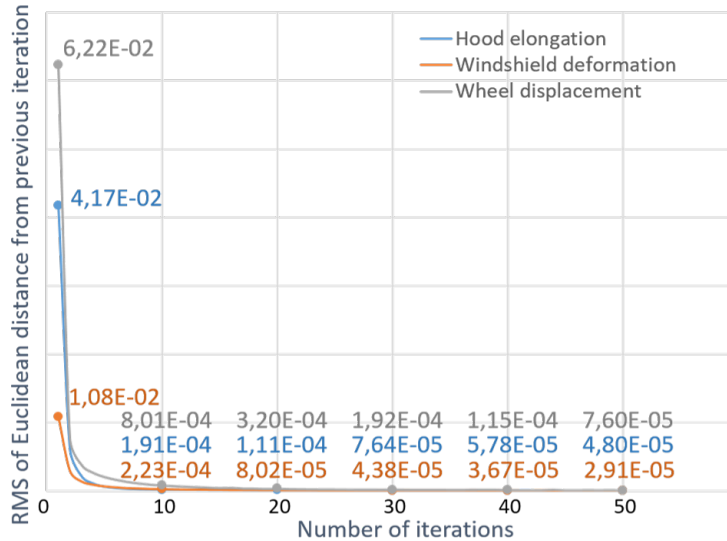
27

Figure 14: Convergence rate observed with test cases of Fig. 12.

is an indication of isotropic and organic behaviors. In contrast, as expected
835 with ASAN, no significant deformation occur in the section planes, see Fig.
13(bottom, middle).

Robustness to choice of handles. The region with large displacements
(dark red region) around $\mathcal{H}$ is indeed quite wide, which means that the user
could place the handle elsewhere in this region without any significant change
840 in the resulting shape. The stiffness distribution around $\mathcal{H}$ gives the user more
flexibility regarding the selection of handles while avoiding adverse effects (see
Sect. 4.4), which eases the interaction for the user, especially in the context of
a design review where modifications must be performed quickly.

Timings & convergence. To compute the weights w_{ij}^{aniso} of ASAN, we only
845 need to add the affine transformation τ of the ROI (Ω) to the ARAP-s&r im-
plementation. This transformation is of linear complexity w.r.t. the number of
vertices, which does not add significant complexity to the overall ASAN defor-
mation process. As an example, for an ROI of around 10K vertices (Figs 10
or 12a), this transformation takes approximately 100ms on a Intel® Core™ i7-
850 6820HQ @2.7 GHz and 32Go of memory.

ARAP-based methods are often regarded as slower than other deforma-
tion methods. Here, especially for car body models where surfaces are rather
stretched, the influence of the convergence is higher. Effectively, the tests per-
formed have shown that the SVD algorithm used in LibIGL to compute the
855 rotation of each vertex neighborhood in single precision floating point numbers,
reached its level of accuracy. Several tens of iterations were needed to obtain ac-
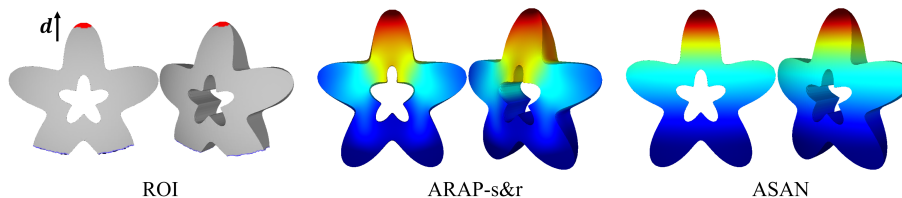curate enough solutions with smooth discrete Gaussian curvature distributions.

28

Figure 15: Elongation of the star model ($\|\mathbf{d}\| = 0.1$). (Left) ROI of initial model with $\mathcal{H}$, $\mathcal{F}$ and $\mathbf{d}$. Results with ARAP-s&r (middle) and ASAN (right) deformation methods, with color plots of the Euclidean distance between Ω and Ω'. ASAN let us preserve the style of the hole without imposing additional constraints.

As shown in Fig. 14, the algorithm converges independently from the mesh size and connectivity. The convergence threshold has been set in accordance with the desired surface quality required by the designers, which led us to 50 iterations, independently of the shape processed.

Other shapes than cars. Figures 15, 16 ans 17 show on normalized models that ASAN deformation could be applied in other design contexts. In Figure 15, the deformation of the star model with ARAP-s&r does not preserve the shape of the hole. Because of the stiffened sections defined with $\mathbf{d}$ and generated over Ω, ASAN highlights a displacement field smoothly distributed from $\mathcal{H}$ over Ω. As a consequence, the style of the hole is preserved without imposing additional constraints.

In Figure 16, we compare ASAN not only to ARAP-s&r implementation but also to ARAP-n (variant of Chen et al. [5]), which computes n-ring neighborhoods in order to obtain some stiffening effect. We take ARAP-n here as a representative of ARAP methods (SR-ARAP, ARAP-h) which all integrate some stiffening effects. A detailed comparison has already been presented in Section 3.3. An artifact appears around $\mathcal{H}$ with ARAP-s&r because its bending stiffness effect is not strong enough. ARAP-n method gives satisfactory results in most cases but it is less predictable and sometimes artifacts appear around $\mathcal{H}$. Moving to ARAP-n increases the stiffening effect but raising n illustrates the saturation effect already mentioned in Fig. 4. Similarly to Fig. 12, ASAN exhibits a predictive behavior without artifact based on its robustness to the choice of handles.

Figure 17 gathers only results obtained with our ASAN method, preserving the sections perpendicular to the user's displacement $\mathbf{d}$. As a result, sharp edges are well preserved through the deformation process. Handles, though defined partly over planar areas, does not lead to deformations of these areas, which illustrates again the robustness of the method with regard to the choice of handles. This is showing how ASAN can cope with extrusion-like deformations of man-made shapes without requiring additional constraints.
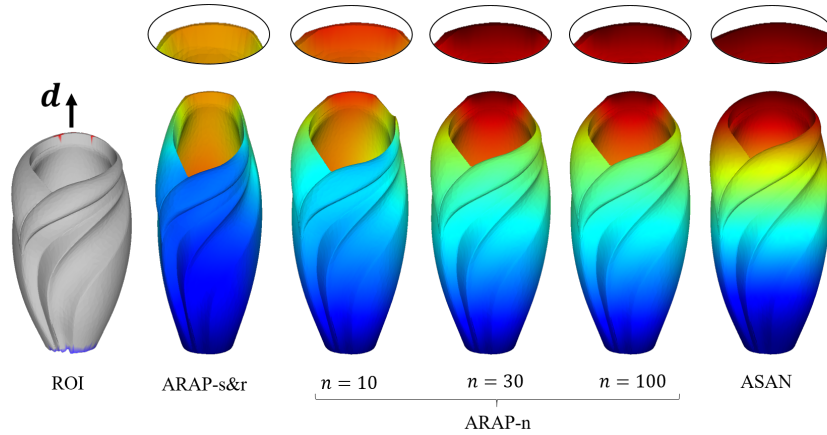
Figure 16: Elongation of a vase ($\|\mathbf{d}\| = 0.1$). Bottom row shows the ROI and color plots of the Euclidean distance between Ω and Ω'. The top row is a zoom on area around $\mathcal{H}$. The result of the ARAP-s&r deformation exhibits an artifact around the handle. ARAP-n does not remove this artifact, even with large vertex neighborhoods, highlighting a saturation effect. ASAN succesfully removes such artifacts.

6. Conclusions & outlook

The results are satisfactory with respect to the requirements set at Sect. 3. The feedback of designers confirmed the quality of the results obtained. The analysis of the mechanical models and the setting of the anisotropic material, combined with already available geometric deformation models, lead to an efficient distribution of stiffness across the deformation area. It appears that studying the physical phenomena associated with a stiffness distribution (see Sect. 4) helps to characterize the possible adverse effects that could arise. Thus, it enables the specification of a stiffness distribution that suits at best the desired deformation (see Sect. 4.4), hence the efficiency of ASAN deformation.

The various test cases show that the ASAN deformation can be reduced to a simple and rather intuitive interaction where the user does not need to monitor complementary parameters than the push/pull direction. Also, the anisotropic material defined effectively acts as a continuous medium, hence it is nonsensitive to the discretization of the deformation area. Therefore, this feature of ASAN deformation can be used over a large range of deformation configurations, irrespective to the mesh gradation, i.e., either coarse of fine.

Further analysis of the designers' requirements can help refining the specification of ASAN deformations. As an example, the evaluation criterion based on discrete Gaussian curvature sign raises questions about areas of null Gaussian curvature that may appear in industrial parts. These areas are particularly sensitive to curvature sign changes and these changes can be sensitive to their orientation w.r.t. to the push/pull direction, eventually producing side effects. This may require further analysis of this phenomenon and tuning of the stiffness of Ω in these particular areas.
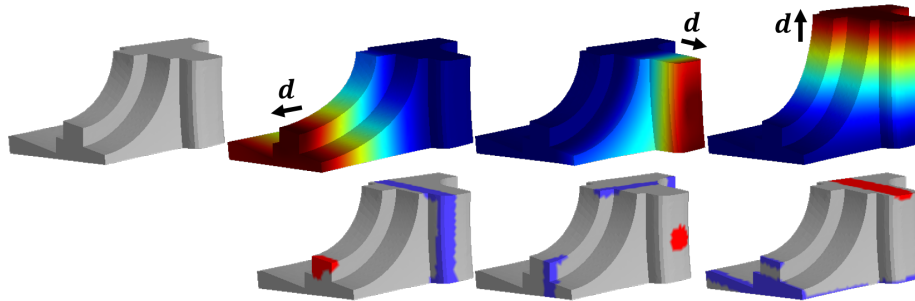
Figure 17: Modifications of the fandisk with our ASAN deformation method. Top row (from left to right): initial model, modifications of the top, side and basis of the model Ω. Results are shown with color plots of the Euclidean distance between Ω and Ω'. Bottom row: location of $\mathcal{H}$ and the fixed constraints of the ROI for each modification of Ω.

Generalizing the deformation schemes to go further than push/pull deformations is still an important issue. The current deformation process covers a subset of the designers' MSS only, and complementary work is needed to address a wider range of shape transformation requirements.

A further improvement could be to provide more control to the user on the definition of the ROI. In our current implementation, we compute the ROI based on handles and fixed vertices positions by simple region growing until $\partial\Omega$ is reached. Furthermore, if the handles are too close to the boundary of the ROI, the deformed surface may differ from the user's expected result. These configurations relate to the cross influence between several boundary conditions in finite elements models. It would improve the user interaction to notice the user in this case.

Sect. 3.3 has highlighted that the stiffness effects claimed in ARAP-based methods cannot be precisely related to mechanical phenomena. While ASAN deformation produces satisfactory results, a more precise adjustment of the stiffness across the deformation area would increase the diversity of deformations needed and cover a wider range of design stages. This is left for future work.

References

[1] C. Bouchard, A. Aoussat, R. Duchamp, Role of sketching in conceptual design of car styling, Journal of Design Research 5 (1) (2006) 116–148.

31

[2] A. Purcell, J. Gero, Drawings and the design process: A review of protocol studies in design and other disciplines and related research in cognitive psychology, Design Studies 19 (4) (1998) 389 – 430.

[3] V. Kokotovich, T. Purcell, Mental synthesis and creativity in design: an experimental examination, Design Studies 21 (5) (2000) 437 – 449.

[4] Z. Levi, G. Gotsman, Smooth rotation enhanced as-rigid-as-possible mesh animation, IEE TVCG 21 (2) (2015) 264:1–277:15.

[5] S.-Y. Chen, L. Gao, Y.-K. Lai, S. Xia, Rigidity controllable as-rigid-as-possible shape deformation, Graphical Models 91 (2017) 13 – 21.

[6] A. Jacobson, L. Kavan, O. Sorkine-Hornung, Robust inside-outside segmentation using generalized winding numbers, ACM Trans. Graph. 32 (4) (2013) 33:1–33:12.

[7] L. Kavan, S. Collins, J. Žára, C. O'Sullivan, Geometric skinning with approximate dual quaternion blending, ACM Trans. Graph. 27 (4) (2008) 105:1–105:23.

[8] O. Sorkine, M. Alexa, As-rigid-as-possible surface modeling, in: Proceedings of the Fifth Eurographics Symposium on Geometry Processing, SGP '07, Eurographics Association, Aire-la-Ville, Switzerland, Switzerland, 2007, pp. 109–116.

[9] A. Jacobson, Algorithms and interfaces for real-time deformation of 2d and 3d shapes, Ph.D. thesis, ETH Zurich (2013).

[10] I. Chao, U. Pinkall, P. Sanan, P. Schröder, A simple geometric model for elastic deformations, ACM Trans. Graph. 29 (4) (2010) 38:1–38:6.

[11] F. Giannini, M. Monti, An innovative approach to the aesthetic design, in: Common Ground–The Design Research Society Conference, 2002, pp. 5–7.

[12] A. Petrov, Understanding the relationships between aesthetic properties of shapes and geometric quantities of free-form curves and surfaces using machine learning techniques, Ph.D. thesis, Paris, ENSAM (2016).

[13] M. E. Yumer, S. Chaudhuri, J. K. Hodgins, L. B. Kara, Semantic shape editing using deformation handles, ACM Trans. Graph. 34 (4) (2015) 86:1–86:12.

[14] I. Kókai, J. Finger, R. C. Smith, R. Pawlicki, T. Vetter, Example-based conceptual styling framework for automotive shapes, in: Proceedings of the 4th Eurographics workshop on Sketch-based interfaces and modeling, ACM, 2007, pp. 37–44.

[15] J. Gain, D. Bechmann, A survey of spatial deformation from a user-centered perspective, ACM Trans. Graph. 27 (4) (2008) 107:1–107:21.

[16] G. Xu, K. Hui, W. Ge, G. Wang, Direct manipulation of free-form deformation using curve-pairs, Computer-Aided Design 45 (3) (2013) 605 – 614.

[17] T. Ju, S. Schaefer, J. Warren, Mean value coordinates for closed triangular meshes, ACM Trans. Graph. 24 (3) (2005) 561–566.

[18] R. Gal, O. Sorkine, N. J. Mitra, D. Cohen-Or, iwires: An analyze-and-edit approach to shape manipulation, ACM Trans. Graph. 28 (3) (2009) 33:1–33:10.

[19] M. Botsch, O. Sorkine, On linear variational surface deformation methods, IEEE Transactions on Visualization and Computer Graphics 14 (1) (2008) 213–230.

[20] D. Sieger, S. Menzel, M. Botsch, Constrained space deformation for design optimization, Procedia Engineering 82 (2014) 114 – 126, 23rd International Meshing Roundtable (IMR23).

[21] H. Zhao, S. J. Gortler, A report on shape deformation with a stretching and bending energy (2016).
URL arXiv:1603.06821

[22] H. Zhao, S. J. Gortler, Shape deformation with a stretching and bending energy, in: Proceedings of the 31st Int. Conf. CASA, Beijing, China, ACM, 2018.

[23] M. Botsch, L. Kobbelt, An intuitive framework for real-time freeform modeling, ACM Trans. Graph. 23 (3) (2004) 630–634.

[24] M. Colaianni, C. Siegl, J. Süßmuth, F. Bauer, G. Greiner, Anisotropic deformation for local shape control, Computational Visual Media 3 (4) (2017) 305–313.

[25] R. W. Sumner, J. Popović, Deformation transfer for triangle meshes, ACM Trans. Graph. 23 (3) (2004) 399–405.

[26] A. Tagliasacchi, T. Delame, M. Spagnuolo, N. Amenta, A. Telea, 3D Skeletons: A State-of-the-Art Report, Computer Graphics Forum 35 (2) (2016) 573–597.

[27] Y. Wang, A. Jacobson, J. Barbič, L. Kavan, Linear subspace design for real-time shape deformation, ACM Trans. Graph. 34 (4) (2015) 57:1–57:11.

[28] O. Zienkiewicz, R. Taylor, The Finite Element Method, 5th Edition, Vol. 1: The Basis, Butterworth Heinemann, 2000.

[29] O. Zienkiewicz, R. Taylor, The Finite Element Method, 5th Edition, Vol. 2: Solid Mechanics, Butterworth Heinemann, 2000.

[30] K. Wisniewski, Finite Rotation Shells: Basic Equations and Finite Elements for Reissner Kinematics, Lecture Notes on Numerical Methods in Engineering and Sciences, Springer, 2010.

[31] L. Gould, Phillip, Analysis of shells and plates, 2nd Edition, Springer Verlag, 1988.

[32] D. Rohmer, S. Hahmann, M.-P. Cani, Exact volume preserving skinning with shape control, in: Proceedings of the 2009 ACM SIGGRAPH/Eurographics Symposium on Computer Animation, SCA '09, ACM, New York, NY, USA, 2009, pp. 83–92.

[33] P. Sanan, Geometric elasticity for graphics, simulation, and computation, Ph.D. thesis, CALTECH, California (2014).

[34] The CGAL Project, CGAL User and Reference Manual, 4.14 Edition, CGAL Editorial Board, 2019.

[35] M. Wardetzky, S. Mathur, F. Kälberer, E. Grinspun, Discrete laplace operators: No free lunch, in: Proceedings of the Fifth Eurographics Symposium on Geometry Processing, SGP '07, Eurographics Association, Aire-la-Ville, Switzerland, Switzerland, 2007.

[36] L. Liu, L. Zhang, Y. Xu, C. Gotsman, S. J. Gortler, A local/global approach to mesh parameterization, in: Proceedings of the Sixth Eurographics Symposium on Geometry Processing, SGP '08, Eurographics Association, Aire-la-Ville, Switzerland, Switzerland, 2008, pp. 1495–1504.

[37] L. Tenek, J. Argyris, Finite Element Analysis for Composite Structures, Vol. 59 of Solid Mechanics And Its Applications, Springer-Science + Business Media, 1998.

[38] U. Pinkall, K. Polthier, Computing discrete minimal surfaces and their conjugates, Experimental Mathematics 2 (1) (1993) 15–36.

[39] O. Sorkine, D. Cohen-Or, Y. Lipman, M. Alexa, C. Rössl, H.-P. Seidel, Laplacian surface editing, in: Proceedings of the EUROGRAPHICS/ACM SIGGRAPH Symposium on Geometry Processing, ACM Press, 2004, pp. 179–188.

[40] A. Jacobson, D. Panozzo, et al., libigl: A simple C++ geometry processing library, http://libigl.github.io/libigl/ (2018).

[41] Pixyz.
URL https://www.pixyz-software.com

[42] Techviz.
URL https://www.techviz.net